journal of the mechanical behavior of biomedical materials 160 (2024) 106721

Contents lists available at ScienceDirect

Journal of the Mechanical Behavior of Biomedical Materials

journal homepage: www.elsevier.com/locate/jmbbm

Characterization of damage mechanisms in cortical bone: Quantification of fracture resistance, critical strains, and crack tortuosity

Anna Gustafsson [a,*], Giulia Galteri [b], Arthur Barakat [a], Jonas Engqvist [c], Lorenzo Grassi [a], Luca Cristofolini [b], Hector Dejea [a,d], Hanna Isaksson [a]

[a] Department of Biomedical Engineering, Lund University, Sweden
[b] Department of Industrial Engineering, Alma Mater Studiorum, University of Bologna, Italy
[c] Division of Solid Mechanics, Lund University, Sweden
[d] MAX IV Laboratory, Lund University, Sweden

ARTICLE INFO

Keywords:
Osteon orientation
Fracture mechanics
DIC
Microcomputed tomography
Microstructure

ABSTRACT

One step towards understanding bone fragility and degenerative diseases is to unravel the links between fracture resistance and the compositional and structural characteristics of cortical bone. In this study, we explore an optical method for automatic crack detection to generate full fracture resistance curves of cortical bone. We quantify fracture toughness, critical failure strains at the crack tip, and crack tortuosity in three directions and analyze how they relate to cortical bone microstructure.

A three-point bending fracture test of single-edge notched beam specimens in three directions (cracks propagating transverse, radial and longitudinal to the microstructure) from bovine cortical bone was combined with 2D-digital image correlation. Crack growth was automatically monitored by analyzing discontinuities in the displacement field using phase congruency analysis. Fracture resistance was analyzed using J-R-curves and strains were quantified at the crack tip. Post-testing, a subset of specimens was scanned using micro-tomography to visualize cracks and to quantify their tortuosity.

Both fracture toughness and crack tortuosity were significantly higher in the transverse direction compared to the other directions. Similar fracture toughness was found for radial and longitudinal directions, albeit 20% higher crack tortuosity in the radial specimens. This suggests that radial crack deflections are not as efficient toughening mechanisms. Strains at crack initiation were ~0.4% for all tissue orientations, while at fully developed damage process zones failure strains were significantly higher in the transverse direction (~1.5%). Altogether, we present unique quantitative data including different aspects of bone damage in three directions, illustrating the importance of cortical bone microstructure.

1. Introduction

Osteoporosis is a disease characterized by low bone mass and fragile bones. In 2019, more than 30 million people in the EU suffered from osteoporosis (Kanis et al., 2021) and it is a major challenge to identify high-risk patients before they fracture, to allow for preventive treatment. In clinical practice, bone mass is used to predict fracture risk. However, there are other key determinants of bone health, apart from bone mass, that are typically overlooked, e.g., the fracture resistance of cortical bone (Dapaah et al., 2023; Hernandez and van der Meulen, 2017). One step towards understanding bone fragility is to unravel the links between fracture resistance and the compositional and structural characteristics of cortical bone. To this, numerous experimental and computational studies have been presented, as covered in (Dapaah et al., 2023; Sabet et al., 2016; Ural, 2020; Wolfram and Schwiedrzik, 2016). Yet, the mechanisms behind the diminished fracture resistance in patients with osteoporosis are not fully known.

The lack of standardized protocols for fracture mechanical testing of cortical bone results in large variability in experimental data and difficulties in comparing data between studies. The tradition of analyzing the fracture toughness of cortical bone goes back more than four decades (Bonfield and Datta, 1976), with a transition from linear to non-linear fracture mechanical testing (Dapaah et al., 2023), as outlined in the ASTM standards E399 (ASTM, 2009) and E1820 (ASTM, 2018). Apart

* Corresponding author. Department of Biomedical Engineering, Lund University, Box 118, 221 00, Lund, Sweden.
E-mail address: anna.gustafsson@bme.lth.se (A. Gustafsson).

https://doi.org/10.1016/j.jmbbm.2024.106721
Received 8 July 2024; Received in revised form 29 August 2024; Accepted 3 September 2024
Available online 5 September 2024

from using different protocols, there is also the option of analyzing single values, e.g., fracture toughness at crack initiation or peak load, or full fracture resistance curves (R-curves) as a function of crack length, which further complicates the comparison between studies (Ritchie et al., 2008). Today, R-curves based on the J-integral are most common for cortical bone, where the crack length is typically estimated from the unloading compliance using empirical relationships (ASTM, 2018). However, as recently discussed by Dapaah and Willett (2022), these protocols were developed for metals, and not bone tissue. They conclude that fracture testing of cortical bone should preferably be done under monotonic loading conditions to avoid viscoelastic effects, such as energy dissipation, due to cyclic loading and partial unloading events. To meet the suggestion of monotonic loading protocols, new methods for tracking the growing crack are needed.

A handful of studies have used imaging techniques to monitor the crack tip in cortical bone, by e.g., performing mechanical testing under a light microscope (Dapaah and Willett, 2022; Shin et al., 2022), a scanning electron microscope (Busse et al., 2013; Shin et al., 2022) or in situ using synchrotron X-ray 2D projections (Zhai et al., 2019, 2020). Common for all these studies is that the crack tip was manually identified from the collected images to monitor the crack growth. A semi-automatic videography method for estimating crack growth was developed by Katsamenis et al. (2013), and later used in other studies (Gauthier et al., 2017; Jenkins et al., 2017; Katsamenis et al., 2015). The approach is to track the whitening front that appears ahead of the crack tip, caused by microdamage in the tissue. This region was identified manually in each image frame and the extent of the region represented a virtual crack tip, which was found to be constantly ~400 μm ahead of the physical crack tip. Yet, fully automatic methods for tracking crack growth are still missing. Sieverts et al. (2022) recently performed in situ fracture testing of cortical bone combined with synchrotron x-ray tomography to capture the crack surface in 3D. They loaded stepwise and stopped the loading to acquire 3D images at each instant when the crack was suspected to grow, based on drops in the load curve. This is a challenging and time-consuming setup, where the number of scans is restricted due to the risk of radiation damage. Hence, the time resolution for analyzing the crack growth and the subsequent data points for R-curve analysis are limited.

Cortical bone exhibits a rising R-curve behavior due to extrinsic toughening mechanisms where growing cracks interact with the microstructure. This results in anisotropic fracture toughness (Zimmermann and Ritchie, 2015). Crack deflections in weak cement line interfaces, seen as irregular and tortuous crack paths, have been identified as important toughening mechanisms particularly when cracks propagate perpendicular to the long axis of osteons in transverse (breaking) directions (Koester et al., 2008; Zimmermann et al., 2009, 2010), but also in the radial (anti-plane longitudinal) (Chan et al., 2009; Katsamenis et al., 2015) direction. Furthermore, lower fracture toughness in aged (Chan et al., 2009; Katsamenis et al., 2015; Koester et al., 2011) or irradiated (Sieverts et al., 2022) bone tissue, and in bone tested at high loading rates (Zimmermann et al., 2014; Zioupos et al., 2020), has been associated with smoother crack surfaces compared to young or quasi-statically loaded tissue. However, the description of the crack surface has been based on qualitative visual inspection, and a quantitative comparison between fracture toughness and crack tortuosity is still lacking.

It is widely accepted that bone damage is strain driven (Nalla et al., 2003), and the development of full-field strain measurements, e.g., using digital image correlation (DIC) or digital volume correlation (DVC), allows for local strain analysis in bone (Dall'Ara and Tozzi, 2022; Grassi and Isaksson, 2015). DIC has been used to study cortical bone damage under tension (Gustafsson et al., 2018), shear (Tang et al., 2015), bending (Dapaah et al., 2020, 2022) and compression (Nguyen et al., 2016), and DVC has been used with in situ testing in compression (Fernández et al., 2020; Koudelka et al., 2021), bending (Sieverts et al., 2022) and using indentation techniques (Fernández et al., 2023; Karali et al., 2021).

Although many different features related to bone damage have been characterized separately in the past, a holistic approach with multiple properties characterized in three directions within the same study is lacking. As an example, only two studies (Nalla et al., 2005; Zhai et al., 2020) characterized the fracture resistance of cortical bone in three anatomical orientations. Due to the large variability in the available experimental data, related to e.g., the choice of test protocol, animal species, anatomical location and age group, it is difficult to do quantitative comparisons between studies and consequently to implement the data into computational models. Such material parameters are crucial for developing computational fracture models that for example can be used to better characterize local properties of osteons and cement lines, currently out of reach using experimental methods.

The aim of this study was to quantify fracture resistance, crack tortuosity and critical strains at the crack tip in three tissue orientations and to investigate potential links between them. We hypothesized that fracture resistance is positively correlated to crack tortuosity and that critical strains at crack initiation are independent of tissue orientation. In order to do so, we propose an experimental approach to fracture mechanical testing including an automatic method for crack detection by analyzing discontinuities in the displacement field from DIC based on (Cinar et al., 2017). With this method, we can explore and compare different loading protocols directly, including both cyclic and monotonic loading, without analyzing the unloading compliance. Additionally, we present an image analysis pipeline to automatically analyze the crack tortuosity from high-resolution tomography images of tested specimens.

2. Methods

2.1. Sample preparation

Three young adult bovine (≈2 years old) femurs were harvested fresh from a local slaughterhouse and stored at −20 °C. Single-edge notched beam (SENB) specimens of cortical bone were cut from the posterior mid-diaphysis of the femurs, which corresponds to the region where Haversian bone is most abundant (Mayya et al., 2016). The SENBs, with the dimension of 2×4×25 mm (thickness × width × length), were cut using a slow diamond band saw (EXAKT 300 CP, Norderstedt, Germany) and during machining, the specimens were constantly irrigated with water. Three orientations were studied (Fig. 1A, Table 1):

- transverse (T) for nominal crack growth transverse to the long axis of the bone, i.e., perpendicular to the long axis of the osteons
- radial (R) for nominal crack growth in the radial direction of the bone (sometimes referred to as anti-plane longitudinal (Nalla et al., 2005))
- longitudinal (L) for nominal crack growth parallel to the long axis of the bone (sometimes referred to as in-plane longitudinal (Nalla et al., 2005))

A sharp notch was prepared perpendicular to the long axis of each specimen, first using the slow diamond band saw (~1.3 mm) and then manually with a scalpel (~0.2 mm). Samples were subsequently wrapped in phosphate buffered saline (PBS) soaked gauze and stored at −20 °C.

The initial notch size a_0 was determined from x-ray microcomputed tomography (μCT) scans (Fig. 1B) taken prior to testing (EasyTom, RX solution, voxel size 29 μm, tube voltage 60 kV). The sharp notch was automatically identified using an in-house MATLAB script (MATLAB R2022a, The MathWorks, Inc.), where the specimens were segmented using thresholding based on Otsu's method (Otsu, 1979) and aligned to the xyz-coordinate system (Fig. 1B). The sharp notch was then identified in each slice and a_0 was calculated as the average notch size over the thickness of the specimen. The average notch size for all samples was 1.47 mm ± 0.16 mm.

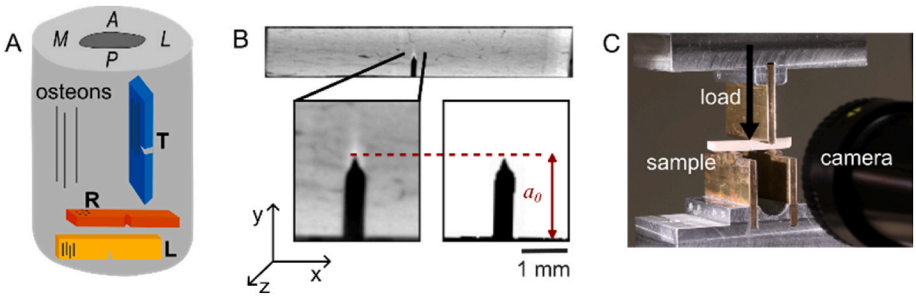

Fig. 1. A) Specimens prepared in three orientations for crack propagation in the transverse (T), radial (R), and longitudinal (L) directions. B) μCT images used to determine the initial notch size a_0. C) Experimental setup with three-point bending and digital image correlation.

Table 1
Overview of number of specimens included in the different tests.

Analysis	Number of specimens in		
	T	R	L
Fracture toughness	**10**	**10**	**9**
Cyclic (+30 μm – 15 μm)	4	4	2
Cyclic (+45 μm – 25 μm)	4	4	5
Monotonic loading	2	2	2
Crack tortuosity	**7**	**6**	**4**

2.2. Fracture testing

We explored three different protocols: cyclic protocols at two different magnitudes (30 μm loading followed by 15 μm unloading, and 45 μm loading followed by 25 μm unloading) and a third protocol where the samples were monotonically loaded until failure (Table 1). In all cases, the three-point bending tests (span length S = 16 mm, Instron 8511 load frame, High Wycombe, UK; MTS Series 793 Control Software, Minneapolis, US) were performed with displacement-controlled loading at 5 μm/s for both loading and unloading events (Fig. 1C). Samples were excluded if 1) the stable crack length before fracture $\Delta a < 0.3$ mm (N = 4) or 2) debris from sample preparation disturbed the digital image correlation at the notch (N = 3). All samples included for the different analyses are presented in Table 1.

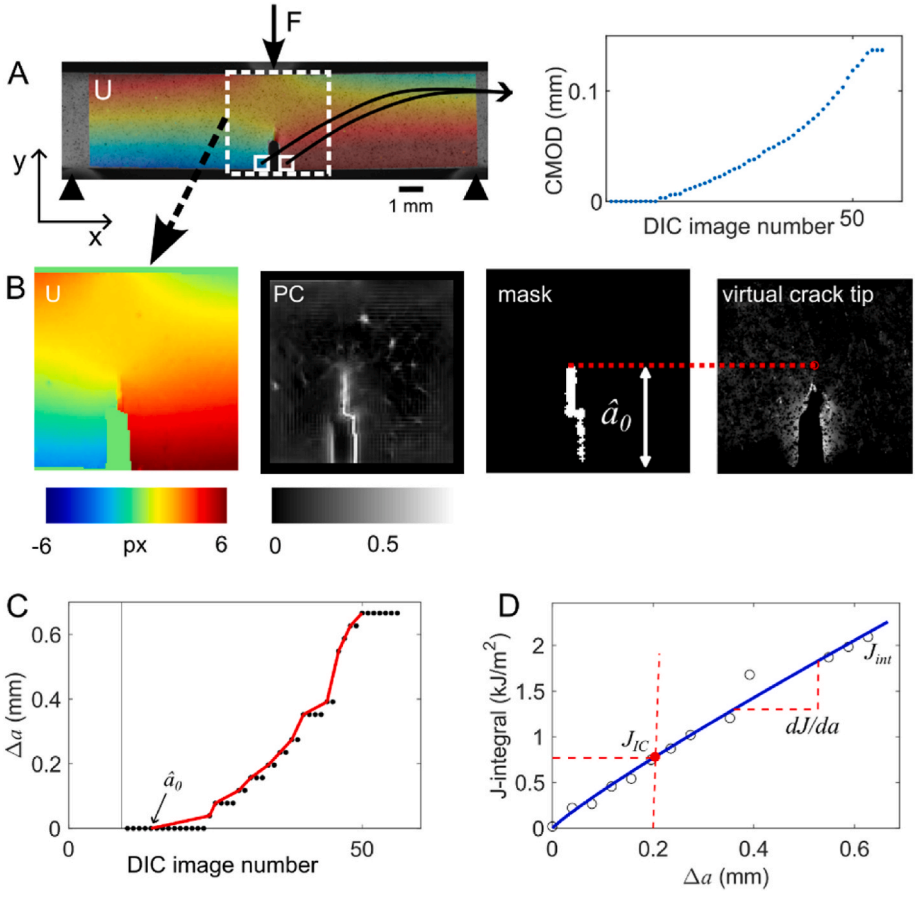

Fig. 2. A) The crack mouth opening displacement (CMOD) was analyzed from the displacement field U in the x-direction. B) An automatic method was developed for detecting cracks by analyzing the phase congruency (PC) of the displacement field (U). C) Crack growth detection from PC analysis of displacement field. Black dots show crack size in all DIC images and red line shows increments with crack growth used for calculating the J-integral. D) J-R curve where a power law (blue) has been fitted to the experimental data (o). The three measures of fracture toughness evaluated are shown: J_{IC}, dJ/da and J_{int}.

2.2.1. Digital image correlation

A digital image system (Vic 2D, Correlated Solution, USA) was used to measure the full-field displacement and calculate the strain distribution throughout the mechanical test. Images were acquired by one camera equipped with a 35 mm lens (Prosilica, GT 6600, 29 Megapixels). A speckle pattern was applied on the surface of each specimen with a black water-based paint using an airbrush. The distance between the specimens and the airbrush air gun was set to 200 mm, while the pressure of the airbrush was set to 4 bars in order to obtain the desired dot size (median dot size was 0.1 mm) (Lionello and Cristofolini, 2014). The images were acquired at 1 frame per second. For DIC analysis, a subset size of 51 pixels and grid spacing of 12 pixels were used, following the nomenclature in (Schreier et al., 2009). For each specimen the strain in the x direction was computed in a zero-strain condition to assess the measurement uncertainty in terms of systematic errors (<1 με) and random errors (<15 με).

The axial strains were then evaluated in two ways: First, by manually identifying the crack tip in the images used for DIC and computing the average strain magnitude in 3×3 points (~10 × 10 μm) at the crack tip. This was done for specimens tested under cyclic loading conditions at two time points: when the specimens reached the maximum load and at the last load cycle before failure. Second, the peak strains at the location of the virtual crack tip (Fig. 2, described in section 2.2.2) were analyzed for all specimens and for all increments where there was an increase in crack size.

2.2.2. Crack monitoring

An automatic method for crack tip detection was implemented following the approach suggested by Cinar et al. (2017). In short, the method builds on the feature that the signal components are in phase (i.e., high phase congruency) at sharp edges in a Fourier representation of an image (Kovesi, 2000b). Cracks can therefore be identified by analyzing the phase congruency (PC) of a displacement field in the frequency domain (Cinar et al., 2017). In our case, the displacement field U normal to the crack (i.e., along the x direction, Fig. 2) was analyzed. First, a square region of interest (ROI) covering the full width of the specimen was selected and centered around the notch. Then, the phase congruency was analyzed on the ROI using Kovesi's PC representation (Kovesi, 2000a, 2000b) that varies between 0 (no phase congruency) and 1. Finally, the crack was segmented using the active contour algorithm (Chan and Vese, 2001) in MATLAB, where the initial mask was automatically obtained by performing non-maximal suppression on the raw PC map (Kovesi, 2000a, 2000b) and then thresholding the output at 70% of the maximum intensity. From the segmented crack, the point with maximum y-coordinate was selected as the virtual crack tip $\hat{a}$. This was done for all increments from the DIC analysis. An overview of the approach is shown in Fig. 2 and in Supplementary Figs. S8–S10.

The physical length scale in the images was determined based on the width W of the corresponding specimen. The number of pixels corresponding to W was determined through an automatic MATLAB script where the upper and lower specimen edges were identified. The pixel size was estimated to be 3.2 μm. With a step size of 12 for DIC, the minimum detectable crack growth was 38.4 μm.

The initial position of the virtual notch $\hat{a}_0$ was determined from the PC analysis and used as a reference for calculating the increase in crack size Δa in the y-direction for each increment. For the cyclic protocols, the initial virtual notch was defined as the average location during the first unloading cycle. Similarly for the monotonic protocol, the increment where 10 N load was reached was identified; the initial virtual notch was defined as the average location between this increment and the ones before and after. The distance between initial physical notch (a_0 in Fig. 1) and initial virtual notch ($\hat{a}_0$ in Fig. 2) was on average 0.56 ± 0.19 mm.

2.2.3. J-resistance (J-R) curve analysis

Crack mouth opening displacement (CMOD) vs load curves were used for fracture resistance analysis. CMOD values were extracted from the displacement field U normal to the crack. The lowermost DIC points at each side of the notch were selected and the local displacements averaged over a neighborhood of 3x3 values (~10 × 10 μm, Fig. 2A) and CMOD was defined as the absolute difference between the displacements of the two points.

Following Dapaah and Willett (2022), the total J-integral at the time step i was computed as

$$J_i = \left(J_{i-1} + \frac{\eta_{i-1}}{Bb_{i-1}} A_{i-1,i}\right)\left(1 - \frac{\gamma_{i-1}}{b_{i-1}}(a_i - a_{i-1})\right) \quad (1)$$

where B is the sample thickness, b_{i-1} is the uncracked ligament length from the previous step, $A_{i-1,i}$ is the net change of the area under the load-CMOD curve at the corresponding time point, and a_i and a_{i-1} are the total crack lengths (including starter notch length) from current and previous steps. Equation (1) is equivalent to the expression in ASTM E1820 (Zhu, 2009), except that the total J-integral is not separated into the elastic (J_{el}) and plastic (J_{pl}) parts as suggested in ASTM E1820. The reason for this is that the unloading compliance needs to be determined to compute J_{el} and J_{pl}, which is not known under monotonic loading conditions. The dimensionless geometry factors η and γ are correction factors accounting for crack growth. For CMOD, they are defined as

$$\eta_{i-1\ (CMOD)} = 3.667 - 2.199\left(\frac{a_{i-1}}{W}\right) + 0.437\left(\frac{a_{i-1}}{W}\right)^2$$

$$\gamma_{i-1\ (CMOD)} = 0.131 + 2.131\left(\frac{a_{i-1}}{W}\right) - 1.465\left(\frac{a_{i-1}}{W}\right)^2$$

The J-integral in (1) was calculated for all increments where there was an increase in crack length. Only increments during the loading periods were included in the analysis. J-R curves (Fig. 2D) were generated where the J-integral was plotted against Δa and a power law $J = c_1(\Delta a)^{c_2}$ was fitted to the experimental data following the standard criteria in ASTM E1820 for what data points to include (ASTM, 2018). Three measures of fracture toughness were calculated: 1) the crack initiation fracture toughness (J_{IC}) calculated as the intersection of the J-integral with a 0.2 mm offset line, 2) the crack propagation fracture toughness (dJ/da) calculated as the slope of the J-R curve at stable crack growth and 3) the instability fracture toughness (J_{int}) which was defined at the last valid point of the J-integral ($\Delta a_{\max} = 0.25 b_0$, where b_0 is the initial intact ligament length) (ASTM, 2018). A comparison between J-integrals based on CMOD and load line displacement (LLD) data were performed for specimens loaded monotonically (see Supplementary Fig. S1).

2.3. Crack tortuosity

A subset of specimens (N = 17, Table 1) was selected to represent characteristic failure modes in each group. The specimens were imaged after testing using high-resolution μCT to analyze the crack tortuosity for the different tissue orientations (Zeiss Xradia, voxel size 6.5 μm, tube voltage 60 kV). The cracks were segmented using a semi-automatic procedure (Fig. 3). All scans were manually rotated to align the specimens with the XY plane using ImageJ (Schneider et al., 2012) and then cropped into small volumes of interest (VOI) containing the notch and crack. The VOIs were binarized through automatic thresholding in ImageJ (Yen et al., 1995) so that the resulting masks included both cracks and tissue porosity (mainly Haversian canals). Next, Haversian canals were identified in MATLAB (R2022a) using a circularity measure, where each segmented feature in the binary volume was tested for circularity $C = P^2/4\pi A$, where P and A are the perimeter and area of a circle. Using this definition, segmented objects with $C < 1.2$ were classified as canals ($C = 1$ corresponds to a perfect circle). This procedure was repeated for x, y and z orientations to account for all canal

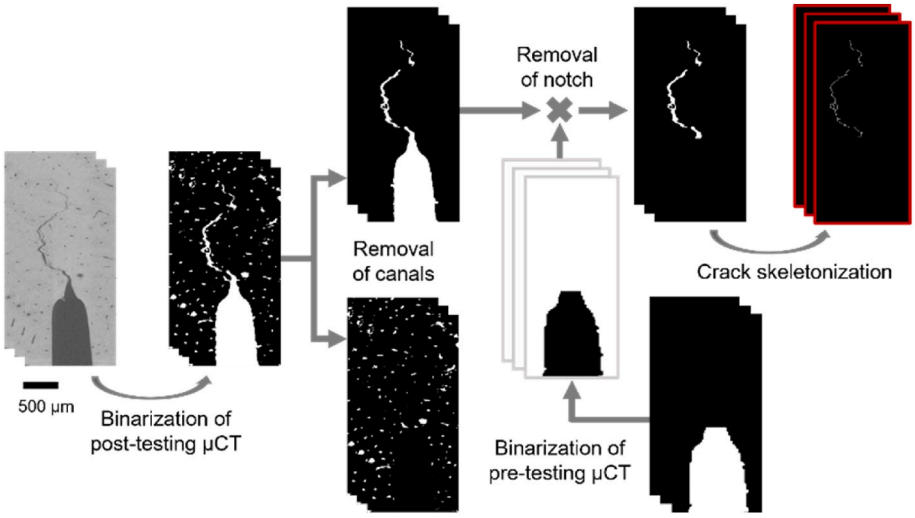

Fig. 3. Overview of crack segmentation method. Pre-processing and binarization were performed in ImageJ and the remaining analysis was performed in MATLAB.

orientations. Any remaining canal, typically interconnected with the crack surface, was segmented manually (SEG3D, CIBC, University of Utah). The initial notch was segmented from the μCT images of the intact specimens. The mask was registered to the images of the tested specimens using a MATLAB built-in intensity-based automatic approach and the notch was removed from the segmented cracks. Finally, the segmented crack was skeletonized into a one-pixel wide centerline preserving the crack topology in 2D. The crack length was calculated as the total perimeter of the skeletonized crack divided by two, using the built-in region properties in MATLAB. The crack tortuosity was then calculated in each 2D image as the total crack length divided by the projected crack length $\Delta a = a - a_0$. For comparison with the fracture toughness parameters, the crack tortuosity was calculated for $\Delta a = 0.25b_0$.

2.4. Statistical analysis

The Shapiro-Wilk test was used to test the normality of the distributions of the analyzed parameters from the J-R curve. A one-way analysis of variance (ANOVA) was used to test for statistical signifi-

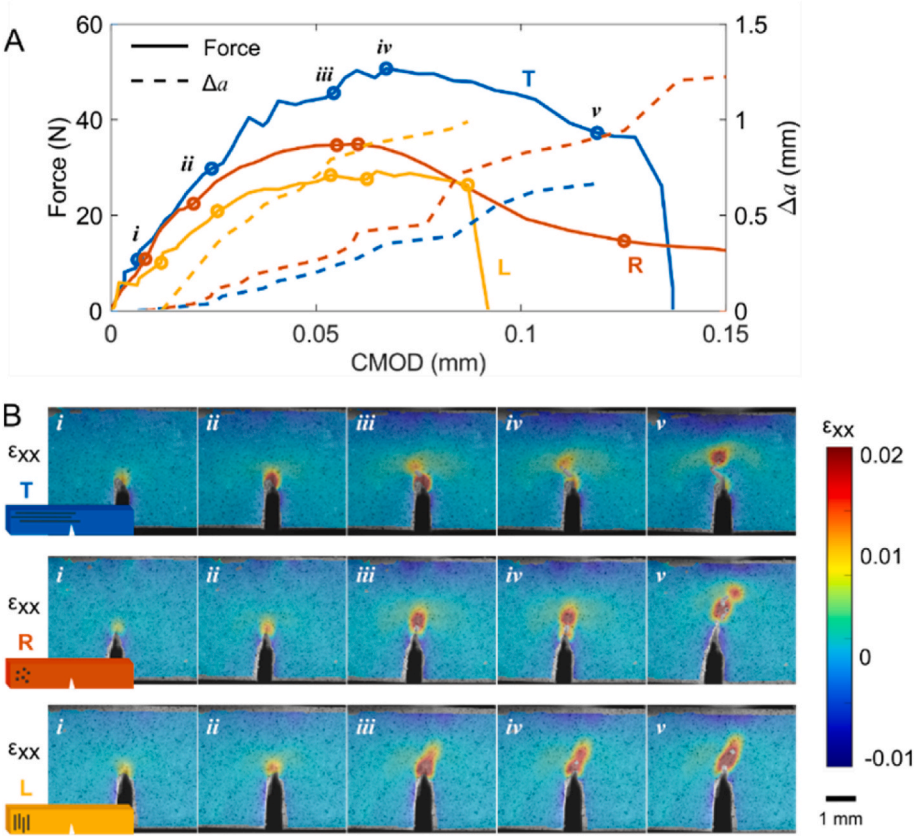

Fig. 4. Representative mechanical data for T, R and L specimens. A) Force vs CMOD curves shown as solid lines and the corresponding crack growth (Δa) vs CMOD shown as dashed lines. B) Strain distributions around the crack tip at five time points (i–v) indicated with circles in the load curves in A.

cance for normally distributed parameters (dJ/da and J_{int}) and the non-parametric Kruskal-Wallis test was used for testing the remaining parameter (J_{IC}). Subsequently, post-hoc contrast tests were performed with Bonferroni corrections to determine significant differences between orientation groups.

Crack tortuosity and peak strains at the virtual crack tip were compared between the orientational groups using linear mixed-effect models. In the first case, crack tortuosity was defined as response variable and orientation (T, R, and L) was used as fixed effect (explanatory variable). For the second case, peak strain was the response variable and tissue orientation (T, R, and L) and crack length (Δa) were used as fixed effects. In both cases, the different specimens were used as a random effect to account for the high number of measurements per specimen. Additionally, protocol type was tested as fixed effect. A Box-Cox transform was applied to both response variables to correct for heteroscedasticity in the residuals. After that, homoscedasticity and normality in the residuals were judged to be met (Supplementary Figs. S3–S6). All statistical analyses were performed in MATLAB (R2022a).

3. Results

Fracture toughness tests in combination with DIC were used to analyze differences between tissue orientations. Typical load-CMOD curves are shown in Fig. 4A, together with the corresponding crack growth curves. Clear differences were seen in load response between groups, where all radial specimens failed in a ductile manner (orange line in Fig. 4A) and all longitudinal specimens failed in a quasi-brittle manner (yellow line in Fig. 4A). Only 4 out of 10 of the transverse specimens showed pronounced softening before failure, comparable to the radial specimens, and the remaining 6 transverse specimens showed modest softening followed by rapid failure (blue line in Fig. 4A). The crack growth was also different between the groups, where both highest crack growth rate (dashed lines in Fig. 4A) and most localized strain concentrations (Fig. 4B) were seen in longitudinal specimens.

The transverse fracture toughness was significantly higher than in the other orientations (Fig. 5). This was true for all three analyzed parameters ($J_{IC}, dJ/da, J_{int}$). The fracture toughness was positively correlated with crack tortuosity ($R^2 = 0.54–0.63$, Fig. 6). The crack tortuosity was highest in transverse specimens and lowest in longitudinal specimens (Fig. 6D). The effect of the different loading protocols was not statistically significant and hence all specimens were pooled per orientation in Fig. 6D. Representative crack patterns and segmented cracks are shown in Fig. 6E.

Strains at the physical crack tip were not significantly different between groups, neither at peak force nor failure (Table 2). However, strains at the virtual crack tip were significantly higher in T specimens compared to R and L (Fig. 7). The linear mixed-effect models also showed that both Δa and Δa^2 were statistically significant effects, while the choice of loading protocol was not. The first bin in Fig. 7 shows peak strain at the virtual crack tip at crack initiation, and here no differences are seen between the groups (mean ± std for T: 0.0043 ± 0.0025, R: 0.0040 ± 0.0024 and L: 0.0039 ± 0.0024).

4. Discussion

In this study, we present a protocol for fracture mechanical testing of cortical bone where we obtained the global response in terms of load-CMOD curves and quantified the tissue fracture toughness from J-R-curves, local failure strains at the virtual crack tip from DIC and the crack tortuosity from μCT. We analyzed three different tissue orientations and hypothesized that fracture resistance was correlated to crack tortuosity. This hypothesis was corroborated for a subset of the specimens imaged with μCT where a positive correlation was confirmed ($R^2 = 0.54–0.63$, Fig. 6). Both fracture toughness and crack tortuosity were highest in the transverse direction. However, the fracture toughness was similar in radial and longitudinal specimens (Fig. 5), although the crack tortuosity in radial orientation was significantly higher than in the longitudinal (Fig. 6D). This shows that crack tortuosity *per se* does not necessarily increase the fracture toughness.

Fracture toughness and toughening mechanisms in cortical bone have been studied extensively using both linear and nonlinear fracture mechanics. In the longitudinal orientation, intact ligaments bridging the crack are the main toughening mechanisms while crack deflection is found to be the predominant toughening mechanisms in radial and transverse orientations (Chan et al., 2009; Gauthier et al., 2020; Katsamenis et al., 2013; Koester et al., 2008; Yan et al., 2007; Zimmermann and Ritchie, 2015). However, most studies focused on one or two orientations and due to the lack of standardized tests for bone, it is difficult to compare data from different studies. Surprisingly few studies analyzed the fracture toughness in all three orientations (T, R and L). Nalla et al. (2005) analyzed human cortical bone using linear elastic fracture mechanics (ASTM E399) and found the critical stress intensity factor K_C to be lowest in R while the total work of fracture was lowest in L. In contrast, Zhai et al. (2020) studied the dynamic fracture toughness (5.4 m/s displacement rate) of porcine bone and found R specimens to have intermediate fracture toughness and explained this by a transition in toughening mechanisms, from crack deflection to ligament bridging. Our results confirm the higher fracture toughness in transverse specimens and show no statistical differences in fracture toughness between radial and longitudinal orientations. Worth noticing is that fracture toughness values for transverse specimens are lower than values reported in a comparable study ($J_{IC} = 2.3$ kJ/m^3 and $J_{int} = 4.1$ kJ/m^2) (Dapaah and Willett, 2022). There can be several reasons for this. First, the method for automatic crack tracking detects the growth of the virtual crack, i.e., the development of the damage process zone, which develops before any visual signs of opening of the physical crack. The

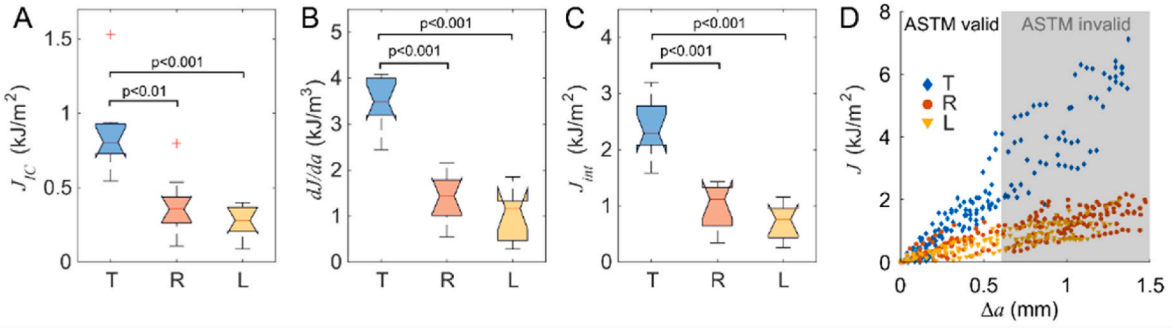

Fig. 5. A-C) Box plots illustrating the fracture toughness parameters estimated from J-R curves. The median value for each group is marked with a horizontal line in the notched boxes, where the lower and upper edges indicate the 25th and 75th percentiles. The whiskers encompass all data points not considered as outliers, which corresponds to 99% coverage for normally distributed data. Outliers beyond whiskers are marked with red +. D) J-R curves for all specimens, where values above the valid ASTM limit $\Delta a_{max} = 0.25 b_0$ have been shaded.

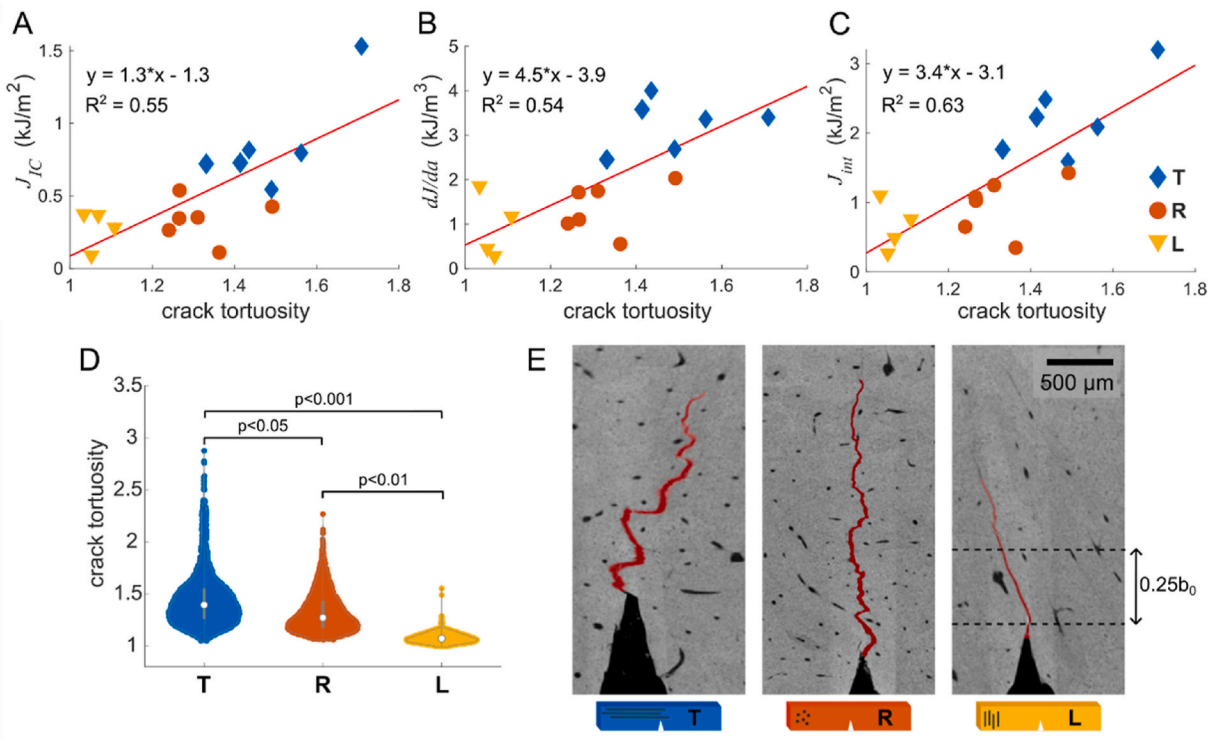

Fig. 6. A-C) Linear regression analysis between fracture mechanics parameters and mean crack tortuosity for each specimen at $\Delta a = 0.25b_0$. D) Violin plots illustrating the distributions of crack tortuosity in the different groups, where each point represents the crack tortuosity in one 2D image. Statistically significant differences between groups are analyzed with linear mixed models. E) Representative crack patterns for the different orientations where the segmented cracks are shown in red and where $\Delta a = 0.25b_0$ is indicated to the right.

Table 2
Strain magnitude at the physical crack tip (mean ± std). No statistically significant differences between groups were observed.

Orientation	Strain at crack tip at peak force	Strain at crack tip at failure
T	0.020 ± 0.004	0.022 ± 0.007
R	0.017 ± 0.006	0.024 ± 0.008
L	0.018 ± 0.005	0.021 ± 0.005

same effect made Katsamenis et al. (2013) raise the question of crack-tip definition in bone. They argued that the damage process zone can be considered as the front-most part of the crack and used to determine the failure resistance. In our case, a comparison with the fracture toughness at physical crack initiation and at maximum load (presented in the supplementary materials, Fig. S7) confirms the differences in fracture toughness for the different tissue orientations as presented in Fig. 5. Second, in the study by Dapaah and Willett (2022), a groove on the back of the samples was machined to enforce a straight mode I crack. In our case, without grooves, cracks could deflect in cement lines and hence follow the path of least resistance. The differences illustrate the importance of the osteon lamellar structure for the fracture toughness of cortical bone, as discussed next.

The hierarchical structure of cortical bone was evident when analyzing the fracture surfaces, with osteons reinforcing the tissue at the millimeter scale and bone lamella forming a plywood structure at the microscale. In the radial direction, cracks tended to follow the weak cement line interfaces and propagated around the osteons in a tortuous but smooth path including multiple deflections (Fig. 8). Rarely did a crack propagate through a Haversian canal, instead, in cases when they penetrated the cement line interface, cracks tended to follow the osteon lamellae. Nucleation of new cracks in cement lines were commonly seen, resulting in intact osteons bridging the different sub-cracks. Similar crack patterns were seen in the longitudinal direction, with smooth cracks following the cement lines, resulting in low tortuosity as osteons were aligned with the load direction. In the longitudinal direction, typical toughening mechanisms with intact lamellae bridging the wake

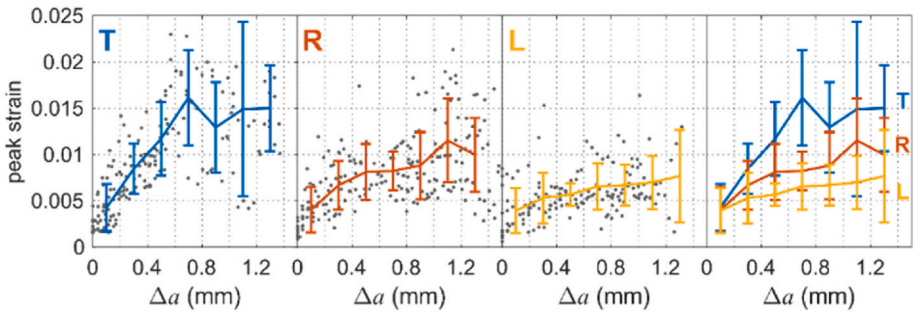

Fig. 7. Peak strains at virtual crack tips at all crack growth increments. All data points have been pooled for each orientational group and strains have been averaged in bins of $\Delta a = 0.2$ mm. Colored bars show mean ± std for each bin.

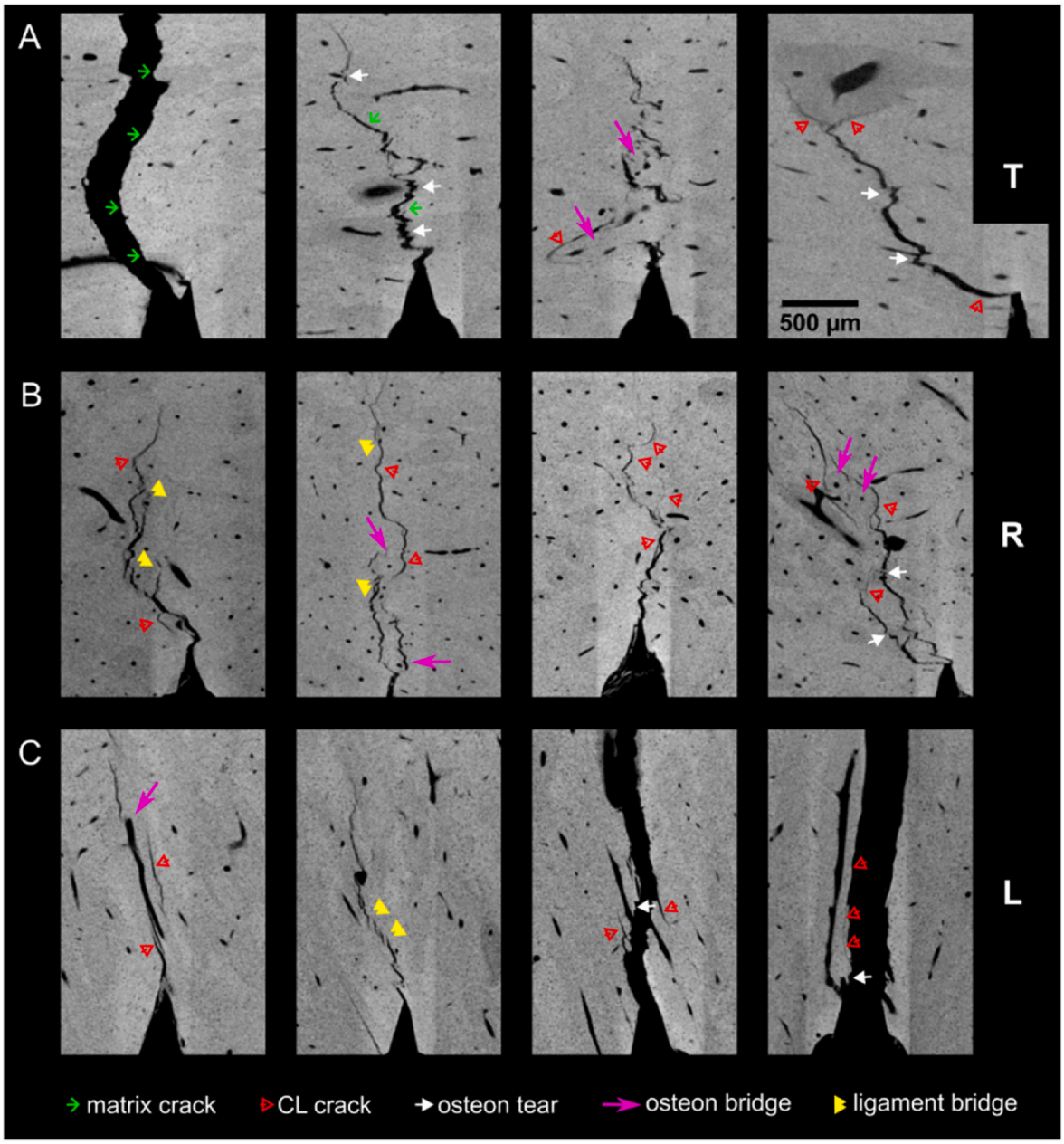

Fig. 8. Representative crack patterns and toughening mechanisms related to the interstitial matrix, osteons and cement lines (CL) in the A) transverse, B) radial and C) longitudinal directions.

of the cracks were also seen (yellow double arrows in Fig. 8). In the transverse direction, sharp crack deflections were seen both at the millimeter scale, when cracks were deflected around the osteons by the cement lines, and at the microscale when propagating perpendicular to the lamellae. The latter phenomenon was particularly obvious for cracks propagating through osteons (white arrows in Fig. 8), where the zig-zag crack pattern was markedly different from the smooth cracks propagating along cement lines (red arrow heads) or through the interstitial matrix (green arrows). We believe this tearing of osteon lamellae to be an important toughening mechanism, especially for transverse specimens (white arrows in Fig. 8). This is in line with a study by Peterlik et al. (2006) that analyzed the fracture toughness of cortical bone as a function of collagen fibril angle and found a sudden transition from brittle (smooth crack surface) to quasi-ductile (zig-zag crack surface) fracture at angles around 50°. The comparison between the radial and longitudinal direction showed that increased crack tortuosity caused by deflections in cement line interfaces did not increase the fracture resistance of the tissue. This is surprising, as crack deflections in cement lines were identified as the main toughening mechanisms in radial samples explaining differences in fracture toughness between young and old cortical bone from human donors (Chan et al., 2009).

The local fracture toughness of osteonal tissue is still not well determined experimentally, as current experimental methods are limited to measuring bulk fracture properties at the tissue scale. Indentation fracture testing suggest that osteons have higher fracture toughness than interstitial matrix, as longer cracks form in matrix compared to osteon tissue for equivalent loads (Mullins et al., 2009). Mathematical models have shown that variations in elastic modulus, as in the osteonal lamella, result in higher apparent fracture resistance compared to the equivalent homogeneous material (Fratzl et al., 2007; Kolednik et al., 2014; Razi et al., 2020). In future studies, computational models can be powerful for estimating local fracture properties using

reverse engineering approaches. Additionally, computational models can be advantageous in analyzing the link between crack deflection and fracture toughness in order to separate the effects of e.g., tissue heterogeneity, anisotropy, and toughening mechanisms arising from smaller length scales. The data set presented in this study will be useful for developing and validating such computational models. It is unique in the sense that it covers all three tissue orientations (T, R and L), including both spatial strain data from DIC, detailed crack topologies from μCT and fracture toughness data, which will enable a level of validation that precedes current literature.

We analyzed failure strains using two different approaches – manually at the physical crack tip and automatically at the virtual crack tip. At the physical crack tip, strain values around 2% were estimated for all different orientations. This is a gross estimation close to the physical crack tip, where the continuity assumption of DIC might be violated. In contrast, looking at the virtual crack tip, strains around 0.4% were found at crack initiation for all orientations, which then increased with increasing crack length until they reached a plateau. This process corresponds to the development of the micro damage process zone, where intrinsic toughening mechanisms take place in front of the physical crack (Willett et al., 2017). Unfortunately, the resolution in the μCT images was insufficient for detecting any micro cracks in front of the physical crack. The size of the process zone was estimated from the start of the strain plateau in Fig. 7 to be ~700 μm in T, ~400 μm in R and ~300 μm in L. This agrees well with previous studies that reported the process zone in cortical bone to be ~550 μm in T (Willett et al., 2017) and ~400 μm in R (Katsamenis et al., 2013). Worth noticing is that the strain magnitude at the front of the process zone seems to be related to the size of the process zone, where the highest plateau strains (~1.5%) were seen in the transverse orientation and the lowest plateau strains in the longitudinal (~0.6%). This reflects the high damage tolerance of cortical bone in the transverse orientation. The process of crack initiation is important for understanding the fracture resistance of bone and future studies should further investigate the processes occurring in the zone between the virtual and physical crack tips.

The most common approach for simulating crack growth in cortical bone using the extended finite element method (XFEM) is to use strain-based damage criteria. To this, the critical strain for crack initiation is a crucial parameter, as this defines when the cohesive crack segment should be introduced in the model. Budyn and Hoc (2007) modelled crack growth in cortical bone using this approach and assumed a critical strain threshold of 0.4% for crack initiation, based on two experimental studies with different scopes: one analyzing the tissue yield strain in trabecular bone (Bayraktar et al., 2004) and one looking at critical damage strain threshold for fatigue loading (Pattin et al., 1996). This assumption by Budyn and Hoc (2007) was followed in multiple subsequent cortical bone XFEM studies (Abdel-Wahab et al., 2012; Gustafsson et al., 2019a, 2019b; Idkaidek and Jasiuk, 2017; Vergani et al., 2014). However, recently we performed a design of experiments study and showed that the critical strain for damage needs to be better determined experimentally. Our results indicated that the critical strain for damage initiation explains around 40% of the variation in maximum force when simulating fracture using XFEM in cortical bone (Gustafsson et al., 2019c). In the current study, we present data indicating that the strain at the virtual crack tip at crack initiation is constant at 0.4% and independent of tissue orientation (Fig. 7).

Cinar et al. (2017) showed that cracks in both quasi-brittle and ductile materials can be identified by analyzing the phase congruency of the displacement field from DIC. Similarly, cracks in trabecular bone have been detected by applying PC analysis to the displacement field from digital volume correlation in 3D (Yan et al., 2020) and by analyzing the von Mises equivalent strain from DIC (Bokam et al., 2020). In this study, we show that PC analysis combined with 2D-DIC can also be used to automatically track stable crack extension in cortical bone. Similar to the videography method developed by Katsamenis et al. (2013), we track the crack growth indirectly by identifying the extent of the micro-damage process zone forming ahead of the crack tip, but in our case based on the displacement field. The proposed method enables the use of monotonic loading protocols for fracture testing of cortical bone, as recommended by Dapaah and Willett (2022). There were no statistically significant differences between fracture parameters from the different loading protocols in our study (see Supplementary Fig. S2). However, this could be due to the limited number of samples. Thus, additional testing is needed in future studies to determine the effects of loading protocols. The minimum detectable increase in crack growth depends both on the frequency of image acquisition and on the settings used for DIC. In our case, it was limited to around 40 μm (3.2 μm image pixel size and a step size of 12 pixels used for DIC). With these settings, the crack was typically identified at the same location for two to four consecutive images during stable crack growth (Fig. 2C), which shows that the image acquisition frequency was not the limiting factor. The crack tip detection was comparable to conventional methods using the unloading compliance for analyzing the J-integral (Dapaah and Willett, 2022; Granke et al., 2015b; Koester et al., 2008). Future studies could try to improve the speckle pattern for DIC by decreasing the size of the speckles and increasing the contrast, possibly trying out other methods than an airbrush for applying the speckles.

Limitations of the study include the use of bovine instead of human tissue. To minimize the differences between the species, all specimens were prepared from the posterior cortices, where the microstructure best resembles human tissue. The small sample size limited the extent of the statistical analysis that could be performed between the different loading protocols (Table 1). However, when comparing different tissue orientations, we still have a high number of samples (N = 29), evenly distributed between groups. This allowed us to analyze the effect of orientation, which was the main focus of the present study. A subset of specimens was selected for post-testing imaging, which might have introduced a bias in the analysis of crack tortuosity. Another limitation was that the testing was conducted in ambient air, instead of submerged in saline solution, due to the video recordings. However, the total time for setup and testing was <10 min for all protocols, comparable to similar protocols (Dapaah and Willett, 2022), which should have minor impact on the results. Short test times is crucial to keep the tissue in a good state, as dehydration is known to decrease the fracture toughness (Granke et al., 2015a; Yan et al., 2008). At all other times, samples were wrapped in PBS-soaked gauze.

In conclusion, we propose a new approach for fracture mechanical testing of cortical bone with automatic optical tracking of the crack growth. The highest fracture toughness was found in the transverse orientation, which was consistent with high crack tortuosity. However, similar fracture toughness was found for radial and longitudinal orientations, albeit higher crack tortuosity in radial specimens. This suggests that crack deflections in weak cement line interfaces in the radial orientation are not as efficient mechanisms for increasing the fracture toughness. Furthermore, we determined the critical strain for damage initiation to be 0.4% in all tissue orientations while strains at the virtual crack tip were significantly higher in the transverse orientation at fully developed damage process zones.

CRediT authorship contribution statement

Anna Gustafsson: Writing – original draft, Supervision, Methodology, Investigation, Funding acquisition, Formal analysis, Conceptualization. **Giulia Galteri:** Writing – review & editing, Methodology, Investigation, Formal analysis. **Arthur Barakat:** Writing – review & editing, Visualization, Investigation. **Jonas Engqvist:** Writing – review & editing, Resources, Methodology. **Lorenzo Grassi:** Writing – review & editing, Methodology. **Luca Cristofolini:** Writing – review & editing, Supervision. **Hector Dejea:** Writing – review & editing, Supervision, Investigation. **Hanna Isaksson:** Writing – review & editing, Supervision, Resources, Methodology, Funding acquisition, Conceptualization.

Declaration of competing interest

The authors declare the following financial interests/personal relationships which may be considered as potential competing interests: Anna Gustafsson reports financial support was provided by Swedish Research Council. Hanna Isaksson reports financial support was provided by Swedish Research Council. Anna Gustafsson reports financial support was provided by Royal Swedish Academy of Sciences. Anna Gustafsson reports financial support was provided by Crafoord Foundation. Anna Gustafsson reports financial support was provided by Foundation of Greta and Johan Kock. If there are other authors, they declare that they have no known competing financial interests or personal relationships that could have appeared to influence the work reported in this paper.

Data availability

Data will be made available on request.

Acknowledgements

This work was supported by the Swedish Research Council [2015–4795, 2019–4517 and 2023–4055], the Royal Swedish Academy of Sciences, the Crafoord Foundation and the Foundation of Greta and Johan Kock. The authors would like to acknowledge the 4D Imaging Lab, Division of Solid Mechanics, Lund University, Lund, for microtomography imaging and Kunal Sharma for technical support.

Appendix A. Supplementary data

Supplementary data to this article can be found online at https://doi.org/10.1016/j.jmbbm.2024.106721.

References

Abdel-Wahab, A.A., Maligno, A.R., Silberschmidt, V.V., 2012. Micro-scale modelling of bovine cortical bone fracture: analysis of crack propagation and microstructure using X-FEM. Comput. Mater. Sci. 52, 128–135. https://doi.org/10.1016/j.commatsci.2011.01.021.

ASTM, 2009. E399-09 Standard Test Tethod for Linear-Elastic Plane-Strain Fracture Toughness of Metallic Materials. American Society for Testing and Materials International, West Conshohocken, PA, USA.

ASTM, 2018. E1820-18: Standard Test Method for Measurement of Fracture Toughness. ASTM International, West Conshohocken, PA, USA.

Bayraktar, H.H., Morgan, E.F., Niebur, G.L., Morris, G.E., Wong, E.K., Keaveny, T.M., 2004. Comparison of the elastic and yield properties of human femoral trabecular and cortical bone tissue. J. Biomech. 37, 27–35. https://doi.org/10.1016/s0021-9290(03)00257-4.

Bokam, P., Germaneau, A., Rigoard, P., Vendeuvre, T., Valle, V., 2020. Evaluation of fracture properties of cancellous bone tissues using digital image correlation/wedge splitting test method. J. Mech. Behav. Biomed. Mater. 102, 103469 https://doi.org/10.1016/j.jmbbm.2019.103469.

Bonfield, W., Datta, P.K., 1976. Fracture toughness of compact bone. J. Biomech. 9, 131. https://doi.org/10.1016/0021-9290(76)90151-2.

Budyn, É., Hoc, T., 2007. Multiple scale modeling for cortical bone fracture in tension using X-FEM. Eur. J. Comput.Mech/Revue Européenne de Mécanique Numérique 16, 213–236.

Busse, B., Bale, H.A., Zimmermann, E.A., Panganiban, B., Barth, H.D., Carriero, A., Vettorazzi, E., Zustin, J., Hahn, M., Ager, J.W., Püschel, K., Amling, M., Ritchie, R.O., 2013. Vitamin D deficiency induces early signs of aging in human bone, increasing the risk of fracture. Sci. Transl. Med. 5 https://doi.org/10.1126/scitranslmed.3006286.

Chan, K.S., Chan, C.K., Nicolella, D.P., 2009. Relating crack-tip deformation to mineralization and fracture resistance in human femur cortical bone. Bone 45, 427–434. https://doi.org/10.1016/j.bone.2009.01.468.

Chan, T.F., Vese, L.A., 2001. Active contours without edges. IEEE T Image Process. 10, 266–277. https://doi.org/10.1109/83.902291.

Cinar, A.F., Barhli, S.M., Hollis, D., Flansbjer, M., Tomlinson, R.A., Marrow, T.J., Mostafavi, M., 2017. An autonomous surface discontinuity detection and quantification method by digital image correlation and phase congruency. Opt Laser. Eng. 96, 94–106. https://doi.org/10.1016/j.optlaseng.2017.04.010.

Dall'Ara, E., Tozzi, G., 2022. Digital volume correlation for the characterization of musculoskeletal tissues: current challenges and future developments. Front. Bioeng. Biotechnol. 10 https://doi.org/10.3389/fbioe.2022.1010056.

Dapaah, D., Badaoui, R., Bahmani, A., Montesano, J., Willett, T., 2020. Modelling the micro-damage process zone during cortical bone fracture. Eng. Fract. Mech. 224 https://doi.org/10.1016/j.engfracmech.2019.106811.

Dapaah, D., Martel, D.R., Iranmanesh, F., Seelemann, C., Laing, A.C., Willett, T., 2023. Fracture toughness: bridging the gap between hip fracture and fracture risk assessment. Curr. Osteoporos. Rep. https://doi.org/10.1007/s11914-023-00789-4.

Dapaah, D., Montesano, J., Willett, T.L., 2022. The importance of rate-dependent effects in modelling the micro-damage process zone in cortical bone fracture. Eng. Fract. Mech. 264 https://doi.org/10.1016/j.engfracmech.2022.108351.

Dapaah, D., Willett, T., 2022. A critical evaluation of cortical bone fracture toughness testing methods. J. Mech. Behav. Biomed. Mater. 134, 105419 https://doi.org/10.1016/j.jmbbm.2022.105419.

Fernández, M.P., Kao, A.P., Witte, F., Arora, H., Tozzi, G., 2020. Low-cycle full-field residual strains in cortical bone and their influence on tissue fracture evaluated via in situ stepwise and continuous X-ray computed tomography. J. Biomech. 113 https://doi.org/10.1016/j.jbiomech.2020.110105.

Fernández, M.P., Schwiedrzik, J., Bürki, A., Peyrin, F., Michler, J., Zysset, P.K., Wolfram, U., 2023. In situ synchrotron radiation μCT indentation of cortical bone: anisotropic crack propagation, local deformation, and fracture. Acta Biomater. 167, 83–99. https://doi.org/10.1016/j.actbio.2023.04.038.

Fratzl, P., Gupta, H.S., Fischer, F.D., Kolednik, O., 2007. Hindered crack propagation in materials with periodically varying Young's modulus - lessons from biological materials. Adv. Mater. 19, 2657. https://doi.org/10.1002/adma.200602394.

Gauthier, R., Follet, H., Langer, M., Meille, S., Chevalier, J., Rongieras, F., Peyrin, F., Mitton, D., 2017. Strain rate influence on human cortical bone toughness: a comparative study of four paired anatomical sites. J. Mech. Behav. Biomed. Mater. 71, 223–230. https://doi.org/10.1016/j.jmbbm.2017.03.015.

Gauthier, R., Follet, H., Langer, M., Peyrin, F., Mitton, D., 2020. What is the influence of two strain rates on the relationship between human cortical bone toughness and micro-structure? Proc. Inst. Mech. Eng. H 234, 247–254. https://doi.org/10.1177/0954411919884776.

Granke, M., Does, M.D., Nyman, J.S., 2015a. The role of water compartments in the material properties of cortical bone. Calcif. Tissue Int. 97, 292–307. https://doi.org/10.1007/s00223-015-9977-5.

Granke, M., Makowski, A.J., Uppuganti, S., Does, M.D., Nyman, J.S., 2015b. Identifying novel clinical surrogates to assess human bone fracture toughness. J. Bone Miner. Res. 30, 1290–1300. https://doi.org/10.1002/jbmr.2452.

Grassi, L., Isaksson, H., 2015. Extracting accurate strain measurements in bone mechanics: a critical review of current methods. J. Mech. Behav. Biomed. Mater. 50, 43–54. https://doi.org/10.1016/j.jmbbm.2015.06.006.

Gustafsson, A., Khayyeri, H., Wallin, M., Isaksson, H., 2019a. An interface damage model that captures crack propagation at the microscale in cortical bone using XFEM. J. Mech. Behav. Biomed. Mater. 90, 556–565. https://doi.org/10.1016/j.jmbbm.2018.09.045.

Gustafsson, A., Mathavan, N., Turunen, M.J., Engqvist, J., Khayyeri, H., Hall, S.A., Isaksson, H., 2018. Linking multiscale deformation to microstructure in cortical bone using in situ loading, digital image correlation and synchrotron X-ray scattering. Acta Biomater. 69, 323–331. https://doi.org/10.1016/j.actbio.2018.01.037.

Gustafsson, A., Wallin, M., Isaksson, H., 2019b. Age-related properties at the microscale affect crack propagation in cortical bone. J. Biomech. 95, 109326 https://doi.org/10.1016/j.jbiomech.2019.109326.

Gustafsson, A., Wallin, M., Khayyeri, H., Isaksson, H., 2019c. Crack propagation in cortical bone is affected by the characteristics of the cement line: a parameter study using an XFEM interface damage model. Biomech. Model. Mechanobiol. 18, 1247–1261. https://doi.org/10.1007/s10237-019-01142-4.

Hernandez, C.J., van der Meulen, M.C., 2017. Understanding bone strength is not enough. J. Bone Miner. Res. 32, 1157–1162. https://doi.org/10.1002/jbmr.3078.

Idkaidek, A., Jasiuk, I., 2017. Cortical bone fracture analysis using XFEM - case study. Int. J. Numer. Method Biomed. Eng. 33 https://doi.org/10.1002/cnm.2809.

Jenkins, T., Katsamenis, O.L., Andriotis, O.G., Coutts, L.V., Carter, B., Dunlop, D.G., Oreffo, R.O.C., Cooper, C., Harvey, N.C., Thurner, P.J., Grp, T.O., 2017. The inferomedial femoral neck is compromised by age but not disease: fracture toughness and the multifactorial mechanisms comprising reference point microindentation. J. Mech. Behav. Biomed. Mater. 75, 399–412. https://doi.org/10.1016/j.jmbbm.2017.06.036.

Kanis, J.A., Norton, N., Harvey, N.C., Jacobson, T., Johansson, H., Lorentzon, M., McCloskey, E.V., Willers, C., Borgström, F., 2021. SCOPE 2021: a new scorecard for osteoporosis in Europe. Arch. Osteoporosis 16. https://doi.org/10.1007/s11657-020-00871-9.

Karali, A., Kao, A.P., Zekonyte, J., Blunn, G., Tozzi, G., 2021. Micromechanical evaluation of cortical bone using XCT indentation and digital volume correlation. J. Mech. Behav. Biomed. Mater. 115 https://doi.org/10.1016/j.jmbbm.2020.104298.

Katsamenis, O.L., Jenkins, T., Quinci, F., Michopoulou, S., Sinclair, I., Thurner, P.J., 2013. A novel videography method for generating crack-extension resistance curves in small bone samples. PLoS One 8, e55641. https://doi.org/10.1371/journal.pone.0055641.

Katsamenis, O.L., Jenkins, T., Thurner, P.J., 2015. Toughness and damage susceptibility in human cortical bone is proportional to mechanical inhomogeneity at the osteonal-level. Bone 76, 158–168. https://doi.org/10.1016/j.bone.2015.03.020.

Koester, K.J., Ager, J.W., Ritchie, R.O., 2008. The true toughness of human cortical bone measured with realistically short cracks. Nat. Mater. 7, 672–677. https://doi.org/10.1038/nmat2221.

Koester, K.J., Barth, H.D., Ritchie, R.O., 2011. Effect of aging on the transverse toughness of human cortical bone: evaluation by R-curves. J. Mech. Behav. Biomed. Mater. 4, 1504–1513. https://doi.org/10.1016/j.jmbbm.2011.05.020.

Koledník, O., Predan, J., Fischer, F.D., Fratzl, P., 2014. Improvements of strength and fracture resistance by spatial material property variations. Acta Mater. 68, 279–294. https://doi.org/10.1016/j.actamat.2014.01.034.
Koudelka, P., Kytyr, D., Fila, T., Sleichrt, J., Rada, V., Zlamal, P., Benes, P., Bendova, V., Kumpova, I., Vopalensky, M., 2021. A method for evaluation the fatigue microcrack propagation in human cortical bone using differential X-ray computed tomography. Materials 14. https://doi.org/10.3390/ma14061370.
Kovesi, P., 2000a. MATLAB and octave functions for computer vision and image processing. https://www.peterkovesi.com/matlabfns.
Kovesi, P., 2000b. Phase congruency: a low-level image invariant. Psychol. Res. Psych. Fo 64, 136–148. https://doi.org/10.1007/s004260000024.
Lionello, G., Cristofolini, L., 2014. A practical approach to optimizing the preparation of speckle patterns for digital-image correlation. Meas. Sci. Technol. 25 https://doi.org/10.1088/0957-0233/25/10/107001.
Mayya, A., Banerjee, A., Rajesh, R., 2016. Haversian microstructure in bovine femoral cortices: an adaptation for improved compressive strength. Mater. Sci. Eng., C 59, 454–463. https://doi.org/10.1016/j.msec.2015.10.047.
Mullins, L.P., Sassi, V., McHugh, P.E., Bruzzi, M.S., 2009. Differences in the crack resistance of interstitial, osteonal and trabecular bone tissue. Ann. Biomed. Eng. 37, 2574–2582. https://doi.org/10.1007/s10439-009-9797-8.
Nalla, R.K., Kinney, J.H., Ritchie, R.O., 2003. Mechanistic fracture criteria for the failure of human cortical bone. Nat. Mater. 2, 164–168. https://doi.org/10.1038/nmat832.
Nalla, R.K., Stolken, J.S., Kinney, J.H., Ritchie, R.O., 2005. Fracture in human cortical bone: local fracture criteria and toughening mechanisms. J. Biomech. 38, 1517–1525. https://doi.org/10.1016/j.jbiomech.2004.07.010.
Nguyen, M.T., Allain, J.M., Gharbi, H., Desceliers, C., Soize, C., 2016. Experimental multiscale measurements for the mechanical identification of a cortical bone by digital image correlation. J. Mech. Behav. Biomed. Mater. 63, 125–133. https://doi.org/10.1016/j.jmbbm.2016.06.011.
Otsu, N., 1979. Threshold selection method from gray-level histograms. IEEE T Syst. Man Cyb. 9, 62–66. https://doi.org/10.1109/Tsmc.1979.4310076.
Pattin, C.A., Caler, W.E., Carter, D.R., 1996. Cyclic mechanical property degradation during fatigue loading of cortical bone. J. Biomech. 29, 69–79. https://doi.org/10.1016/0021-9290(94)00156-1.
Peterlik, H., Roschger, P., Klaushofer, K., Fratzl, P., 2006. From brittle to ductile fracture of bone. Nat. Mater. 5, 52.
Razi, H., Predan, J., Fischer, F.D., Koledník, O., Fratzl, P., 2020. Damage tolerance of lamellar bone. Bone 130. https://doi.org/10.1016/j.bone.2019.115102.
Ritchie, R.O., Koester, K.J., Ionova, S., Yao, W., Lane, N.E., Ager, J.W., 2008. Measurement of the toughness of bone: a tutorial with special reference to small animal studies. Bone 43, 798–812. https://doi.org/10.1016/j.bone.2008.04.027.
Sabet, F.A., Raeisi Najafi, A., Hamed, E., Jasiuk, I., 2016. Modelling of bone fracture and strength at different length scales: a review. Interface Focus 6, 20150055. https://doi.org/10.1098/rsfs.2015.0055.
Schneider, C.A., Rasband, W.S., Eliceiri, K.W., 2012. NIH Image to ImageJ: 25 years of image analysis. Nat. Methods 9, 671–675.
Schreier, H., Orteu, J.-J., Sutton, M.A., 2009. Image Correlation for Shape, Motion and Deformation Measurements: Basic Concepts, Theory and Applications. Springer.
Shin, M., Zhang, M., vom Scheidt, A., Pelletier, M.H., Walsh, W.R., Martens, P.J., Kruzic, J.J., Busse, B., Gludovatz, B., 2022. Impact of test environment on the fracture resistance of cortical bone. J. Mech. Behav. Biomed. Mater. 129 https://doi.org/10.1016/j.jmbbm.2022.105155.
Sieverts, M., Obata, Y., Rosenberg, J.L., Woolley, W., Parkinson, D.Y., Barnard, H.S., Pelt, D.M., Acevedo, C., 2022. Unraveling the effect of collagen damage on bone fracture using in situ synchrotron microtomography with deep learning. Commun. Mater. 3 https://doi.org/10.1038/s43246-022-00296-6.
Tang, T., Ebacher, V., Cripton, P., Guy, P., McKay, H., Wang, R., 2015. Shear deformation and fracture of human cortical bone. Bone 71, 25–35. https://doi.org/10.1016/j.bone.2014.10.001.
Ural, A., 2020. Advanced modeling methods-applications to bone fracture mechanics. Curr. Osteoporos. Rep. 18, 568–576. https://doi.org/10.1007/s11914-020-00615-1.
Vergani, L., Colombo, C., Libonati, F., 2014. Crack propagation in cortical bone: a numerical study. In: 20th European Conference on Fracture, 3, pp. 1524–1529. https://doi.org/10.1016/j.mspro.2014.06.246.
Willett, T., Josey, D., Lu, R.X.Z., Minhas, G., Montesano, J., 2017. The micro-damage process zone during transverse cortical bone fracture: No ears at crack growth initiation. J. Mech. Behav. Biomed. Mater. 74, 371–382. https://doi.org/10.1016/j.jmbbm.2017.06.029.
Wolfram, U., Schwiedrzik, J., 2016. Post-yield and failure properties of cortical bone. BoneKEy Rep. 5, 829. https://doi.org/10.1038/bonekey.2016.60.
Yan, J., Mecholsky Jr., J.J., Clifton, K.B., 2007. How tough is bone? Application of elastic-plastic fracture mechanics to bone. Bone 40, 479–484. https://doi.org/10.1016/j.bone.2006.08.013.
Yan, J.H., Daga, A., Kumar, R., Mecholsky, J.J., 2008. Fracture toughness and work of fracture of hydrated, dehydrated, and ashed bovine bone. J. Biomech. 41, 1929–1936. https://doi.org/10.1016/j.jbiomech.2008.03.037.
Yan, L.Y., Cinar, A., Ma, S.C., Abel, R., Hansen, U., Marrow, T.J., 2020. A method for fracture toughness measurement in trabecular bone using computed tomography, image correlation and finite element methods. J. Mech. Behav. Biomed. Mater. 109 https://doi.org/10.1016/j.jmbbm.2020.103838.
Yen, J.C., Chang, F.J., Chang, S., 1995. A new criterion for automatic multilevel thresholding. IEEE Trans. Image Process. 4, 370–378. https://doi.org/10.1109/83.366472.
Zhai, X., Guo, Z., Gao, J., Kedir, N., Nie, Y., Claus, B., Sun, T., Xiao, X., Fezzaa, K., Chen, W.W., 2019. High-speed X-ray visualization of dynamic crack initiation and propagation in bone. Acta Biomater. 90, 278–286. https://doi.org/10.1016/j.actbio.2019.03.045.
Zhai, X.D., Nie, Y.Z., Gao, J.L., Kedir, N., Claus, B., Sun, T., Fezzaa, K., Chen, W.W., 2020. The effect of loading direction on the fracture behaviors of cortical bone at a dynamic loading rate. J. Mech. Phys. Solid. 142 https://doi.org/10.1016/j.jmps.2020.104015.
Zhu, X.K., 2009. J-Integral Resistance Curve Testing and Evaluation, vol. 10. J Zhejiang Univ-Sc A, pp. 1541–1560. https://doi.org/10.1631/jzus.A0930004.
Zimmermann, E.A., Gludovatz, B., Schaible, E., Busse, B., Ritchie, R.O., 2014. Fracture resistance of human cortical bone across multiple length-scales at physiological strain rates. Biomaterials 35, 5472–5481. https://doi.org/10.1016/j.biomaterials.2014.03.066.
Zimmermann, E.A., Launey, M.E., Barth, H.D., Ritchie, R.O., 2009. Mixed-mode fracture of human cortical bone. Biomaterials 30, 5877–5884. https://doi.org/10.1016/j.biomaterials.2009.06.017.
Zimmermann, E.A., Launey, M.E., Ritchie, R.O., 2010. The significance of crack-resistance curves to the mixed-mode fracture toughness of human cortical bone. Biomaterials 31, 5297–5305. https://doi.org/10.1016/j.biomaterials.2010.03.056.
Zimmermann, E.A., Ritchie, R.O., 2015. Bone as a structural material. Adv. Healthcare Mater. 4, 1287–1304. https://doi.org/10.1002/adhm.201500070.
Zioupos, P., Kirchner, H.O.K., Peterlik, H., 2020. Ageing bone fractures: the case of a ductile to brittle transition that shifts with age. Bone 131, 115176. https://doi.org/10.1016/j.bone.2019.115176.